

Image-Based Macro-Micro Finite Element Models of a Canine Femur with Implant Design Implications

Somnath Ghosh , Ganapathi Krishnan & Jonathan Dyce

To cite this article: Somnath Ghosh , Ganapathi Krishnan & Jonathan Dyce (2006) Image-Based Macro-Micro Finite Element Models of a Canine Femur with Implant Design Implications, International Journal for Computational Methods in Engineering Science and Mechanics, 7:3, 155-171, DOI: [10.1080/15502280500387831](https://doi.org/10.1080/15502280500387831)

To link to this article: <http://dx.doi.org/10.1080/15502280500387831>



Published online: 23 Feb 2007.



Submit your article to this journal [↗](#)



Article views: 59



View related articles [↗](#)

Image-Based Macro-Micro Finite Element Models of a Canine Femur with Implant Design Implications

Somnath Ghosh, Ganapathi Krishnan, and Jonathan Dyce

Department of Mechanical Engineering, The Ohio State University, Columbus, Ohio, USA

In this paper, a comprehensive model of a bone-cement-implant assembly is developed for a canine cemented femoral prosthesis system. Various steps in this development entail profiling the canine femur contours by computed tomography (CT) scanning, computer aided design (CAD) reconstruction of the canine femur from CT images, CAD modeling of the implant from implant blue prints and CAD modeling of the interface cement. Finite element analysis of the macroscopic assembly is conducted for stress analysis in individual components of the system, accounting for variation in density and material properties in the porous bone material. A sensitivity analysis is conducted with the macroscopic model to investigate the effect of implant design variables on the stress distribution in the assembly. Subsequently, rigorous microstructural analysis of the bone incorporating the morphological intricacies is conducted. Various steps in this development include acquisition of the bone microstructural data from histological serial sectioning, stacking of sections to obtain 3D renderings of void distributions, microstructural characterization and determination of properties and, finally, microstructural stress analysis using a 3D Voronoi cell finite element method. Generation of the simulated microstructure and analysis by the 3D Voronoi cell finite element model provides a new way of modeling complex microstructures and correlating to morphological characteristics. An inverse calculation of the material parameters of bone by combining macroscopic experiments with microstructural characterization and analysis provides a new approach to evaluating properties without having to do experiments at this scale. Finally, the microstructural stresses in the femur are computed using the 3D VCFEM to study the stress distribution at the scale of the bone porosity. Significant difference is observed between the macroscopic stresses and the peak microscopic stresses at different locations.

Keywords Computed Tomography, CAD, Material Properties, FEM Bone Microstructure, Voronoi Cell Finite Element Model, Material Characterization

1. INTRODUCTION

Disabling and intractably painful degenerative hip disease is common in human beings and dogs, as discussed in Olmstead [1]. Total hip replacement is now routinely performed in both species and offers an excellent prognosis for improved and comfortable function. In human beings, aseptic loosening is the principal mechanism of prosthetic failure and is associated with considerable patient morbidity. Approximately 10% of patients will require surgical revision for aseptic loosening within 15 years of installation [2]. In cemented total hip replacement, a mantle of polymethylmethacrylate (PMMA) anchors the femoral prosthesis, and distributes stresses from the femoral stem to the surrounding bone [3]. If stresses in the bone-implant interface are excessive, osteolysis or stress fracture will occur. Figure 1 shows the X-rays of an implanted hip and the image of a stress fracture in the cement mantle, respectively. The quality of the cement mantle and the orientation of the femoral stem as determinants of aseptic loosening and modern cementing techniques have been described [4, 5]. In a review of cementing techniques, Poss et al. [6] have concluded that prosthetic designs and surgical techniques that combine optimal use of cement and appropriate load transfer should confer successful long-term results in total hip arthroplasty. In canine orthopedics, there is currently debate regarding the optimal position, shape, size and mantle properties for a cemented femoral prosthesis [7]. Concern regarding femur fracture and high incidence of failure in total hip replacement procedures has led to a number of intuitive proposed design changes such as shortening of the stem embarkations on the cranial and caudal surfaces, reduced stem diameter, and a flattened lateral cross section.

The finite element method has emerged as a powerful tool for modeling various complex biomedical systems. For modeling implants and other surgical processes, this method has been used to design devices that effectively reduce stress distributions in

Received 19 December 2003; accepted 8 July 2005.

This work has been supported by an Interdisciplinary Biomaterials Seed Grant (IBSG) by the Office of Research at the Ohio State University. The implant designs have been provided by BioMedtrix Inc. Their help is gratefully acknowledged. The authors are grateful to the technical staff in the department of Veterinary Medicine and Veterinary Biosciences for their help with the experiments. Computer support by the Ohio Supercomputer Center through grant # PAS813-2 is also acknowledged.

Address correspondence to Somnath Ghosh, Department of Mechanical Engineering, The Ohio State University, 650 Ackerman Road, Suite 255, Columbus, OH 43202, USA. E-mail: ghosh.5@osu.edu

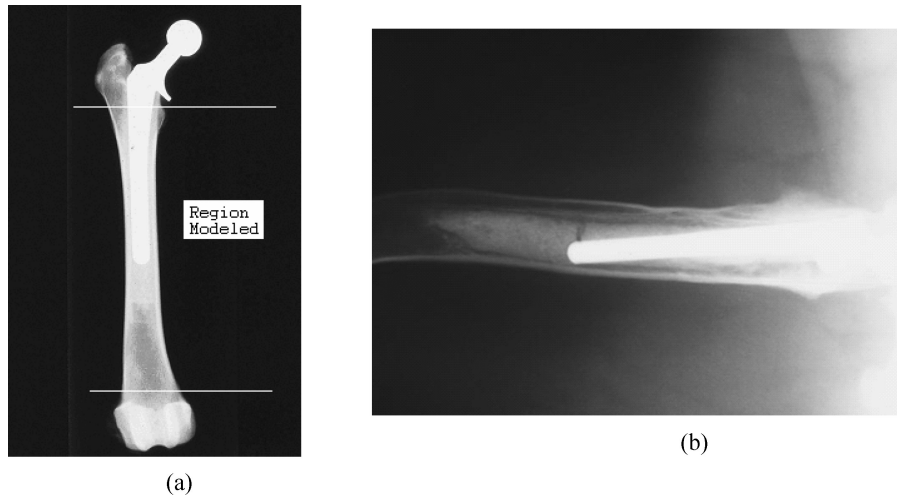


FIG. 1. X-ray images (a) of an implanted femur, (b) of stress fracture in the cement mantle.

the bone [8–10]. FEM modeling of prostheses under various load conditions has reduced the need for complex and expensive laboratory and in vivo tests. However, a few key limitations have restricted the widespread use of these prostheses by orthopedic surgeons and implant manufacturers.

- (i) A number of these analyses make two dimensional plane strain, plane stress or axi-symmetric assumptions to enhance modeling efficiency and reduce costs. In reality, the complex bone geometry, as well as the nature of physiological loading, makes these assumptions inadequate from a functional standpoint. A complete 3D model, with geometric details of the prosthesis, bone anatomy and physiologically correct loads, is necessary to make reliable predictions.
- (ii) An inherent complexity of the endoprosthesis is the involvement of three different materials, viz. bone, cement, and metal. While the material of the cement and metallic implants may be assumed to be homogeneous enough, the bone material is quite heterogeneous in nature. Bone has been modeled with phenomenological constitutive relations that have linear variability, elasticity and anisotropy, e.g. in [9, 10]. While these models are capable of predicting macroscopic behavior, they are generally incapable of capturing material behavior at the microstructural level, such as microscopic stress concentration, crack evolution at the scale of the bone porosity. Models employing effective moduli have used “unit cell models” with average bone porosity, e.g. Ashman [11]. Impediments to detailed microstructural models are lack of (a) robust methods of image-based modeling, in which morphological characteristics are mapped directly to the analysis model, and (b) efficient analysis tools for modeling complex microstructural regions.
- (iii) A frequent assumption in bone analysis is that material constitution does not change appreciably from one macro-

scopic location to another. Limitations in experimental evaluation necessitate this assumption and thus they do not account for spatial variability in material properties.

- (iv) Finite element models have been used to design the shape and materials of the femoral stem, and to improve cement mantle stresses in [8, 12] have recommended a non-uniform mantle that is thicker distally about a tapered stem, while a uniform mantle has been favored in [13]. This disparity is a consequence of the lack of robust design methodology. There is agreement on the opinion that cement stresses are the highest in the proximal medial and distal lateral regions. Estok et al. [14] have concluded that an important factor influencing strains in the mantle near the tip of the prosthesis is a thin mantle.

This work is aimed at developing a comprehensive approach for stress analysis at different scales of the bone-cement-implant assembly in a canine femur with implications on implant design. The first part of the paper deals with macroscopic modeling through a systematic integration of (i) profiling femur contours by CT scanning, (ii) 3D CAD reconstruction of the bone, implant and cement from CT images and blue prints, (iii) macro-scale finite element analysis of the bone-cement-implant assembly, and (iv) study on the effect of design changes to the implant on the stresses. The second part utilizes methods of microstructural characterization and stress analysis to understand the sensitivity of microstructural stress distribution to local morphological parameters such as volume fraction, size, shape and spatial distribution of porosities. Microstructural models are developed to be morphologically equivalent to micrographs obtained from histology. Steps followed in this development include acquisition of bone microstructural data from histology, 3D renderings of void distributions, 3D microstructure characterization, determination of material properties, and microstructural stress analysis.

2. MODEL OF THE CANINE FEMUR-CEMENT-IMPLANT ASSEMBLY

2.1. CT Scanning of the Femur

The complex geometric structure of the canine femur strongly influences the mechanical behavior of the bone-cement-implant assembly. Various methods have been proposed to determine bone morphology for 3D solid modeling. Computed tomography (CT), which uses X-ray to create slices containing detailed cross sectional images of the body, is currently used extensively as a diagnostic tool in biomedical research due to accuracy, high resolution (~ 0.1 mm), and ease and cost-effectiveness of data extraction. CT scans have been used for 3D bone modeling in many studies, e.g. [10, 15]. This is used in the development of 3D models of bone-cement-implant assembly.

A typical femur is shown in Fig. 2a, for which the proximal end presents a smooth, nearly hemispherical head supported by a neck, while the distal end is quadrangular and protrudes caudally. The shaft or diaphysis of the femur is nearly cylindrical, and is straight proximally and cranially bowed distally. In constructing the CT images of the femur, contiguous transaxial images are acquired using a Picker QRS helical CT scanner with acquisition parameters of voxel slice density as 512×512 , and slice collimation as 1 mm. Images are acquired using high-pass bone filter and the smallest possible field of view. The femur of length 196 mm is scanned using an inter-slice distance of 1 mm CT sections at various locations along the length of the bone are depicted in Fig. 2b. There is a significant variation in the cross-sectional topology from the proximal to the distal region.

It has a significantly greater width in the metaphysial regions than in the diaphysial region, while the cortical bone is observed to be of higher density than the cancellous bone.

2.2. CAD Based Construction of the 3D Femur Model

The bone sections acquired through CT are imported into AutoCAD[®] 2000, a commercial 2D design and drafting platform with a direct interface with the CT data. Each of the CT sections is retraced in AutoCAD[®] [16] and saved in the IGES (Initial Graphics Exchange Specification) format. This procedure enables the CT sections to be exported to I-DEAS[™] [17], a solid modeling package used in constructing the 3D bone model. The finite element analysis excludes the femoral head and the distal condyles, and hence only 156 out of the 196 CT sections are utilized. In IDEAS[™], the working plane is set up perpendicular to the longitudinal direction of the bone. The working plane is moved to coincide with the plane of the imported bone section each time a new section is introduced.

Definition of a bone section is facilitated by using the “surface by boundary” function in IDEAS[™] [17] Master Modeler Module. The bone section is translated to the actual physical location along the length of the bone based on the 3D CT data. This procedure results in a series of 2-D bone sections stacked along its length, as shown in Fig. 3a. The “lofting” tool in I-DEAS[™] is used to combine sections for developing the composite 3D bone model depicted in Fig. 3b. This tool linearly interpolates between the slices at 1 mm interval and stitches together a sequence of 2D sections with minimum distortion. Sections of the 3D models at various locations are compared with the actual

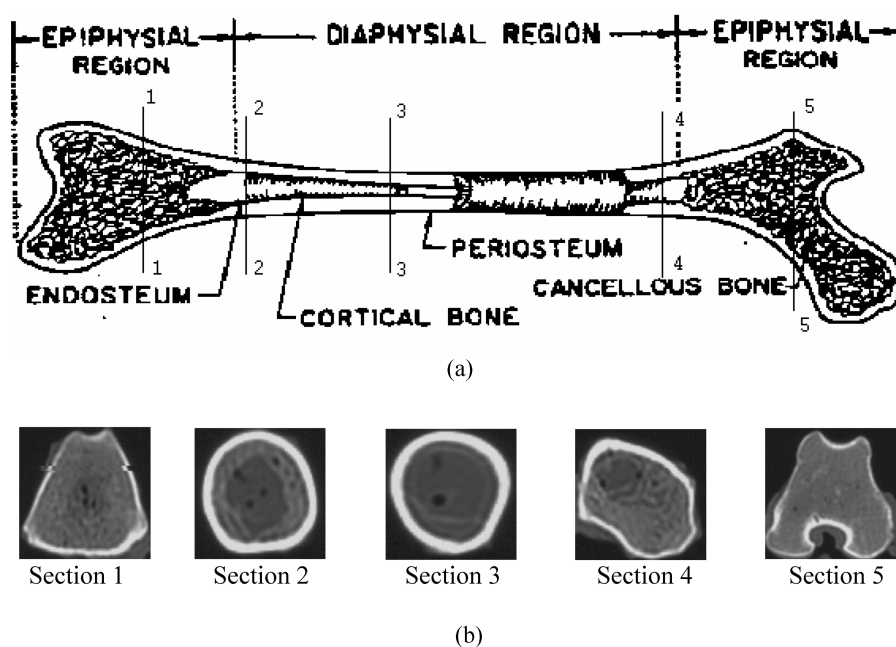


FIG. 2. (a) Illustration of different regions in the femur; (b) CT sections at different regions.

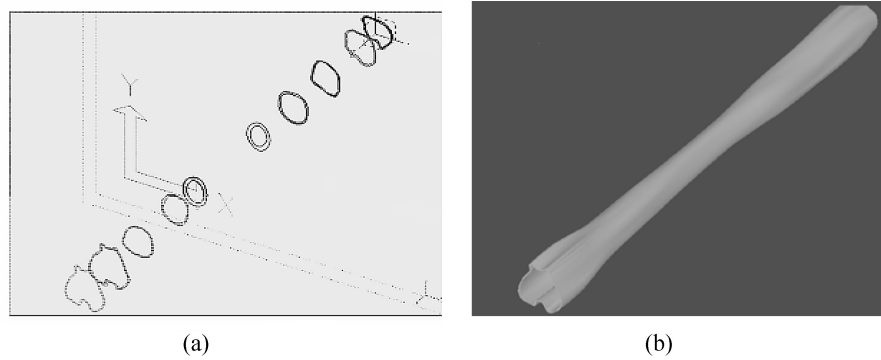


FIG. 3. (a) Stacking a series of bone sections in IDEAS Master Modeler; (b) 3D solid model of the canine femur.

CT data by superimposing on the CT images and good match is obtained between images.

2.3. CAD Model of the Implant Model and Interfacial Cement Mantle

As shown in Fig. 1a, a typical implant used in cemented hip replacements consists of a femoral head and stem. It is made of stainless steel, cobalt chromium or titanium alloys, with an acetabular cup composed of ultra-high molecular weight polyethylene (UHMWPE). The shape of the stem is critical in the design of the femoral components, since it has to facilitate adequate blending with the proximal femur to restore normal joint kinematics and to minimize the risk of implant failure and bone loss. Load transfer from the implant to the cement and the bone is affected by cross-sectional shape, stem length and geometric configuration. Sharp corners increase stress concentration, leading to cement cracking. The cobalt chrome implant modeled in this study (see Fig. 4a) is designed and manufactured by Biomedtrix Corporation [18]. A solid model of the implant is developed from BioMedrix's blueprints using I-

DEASTM as shown in Fig. 5a. The femoral head is excluded from the analysis and hence the collar, neck, and head of the implant are not modeled. Studies [19] have shown that an increase in stem length reduces the compressive stresses in the bone. Consequently, a range of implant sizes is modeled to understand the effect of stem length on the compressive stresses in the bone.

In a cemented total hip replacement system, the cement anchors the implant in position and fills the annular region between the implant and the bone. Mapping this annular region for modeling the cement is quite complex. The bone and the implant are assembled in I-DEASTM Master Assembler Module such that the distal tip is centrally located, providing a uniform cement mantle in the distal region of the femur. In actual practice, the same objective is achieved by using an injection molded PMMA distal stem centralizer. The outer surface of the implant and the inner surface of the bone are extracted using a surface extraction tool, which traces the outer cross section of the implant at 1 mm intervals. The extracted surfaces are then stitched together using the "lofting" tool in I-DEASTM as shown in Fig. 5b. In most cases the cement mantle extends beyond the length of the

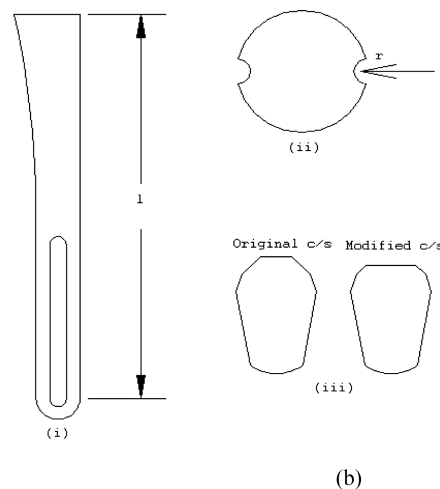
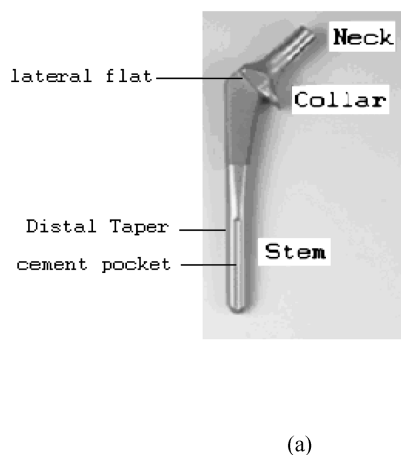


FIG. 4. (a) Prosthetic implant manufactured by Biomedtrix Co, (b) design for the implant including distal taper length, cemented pocket depth and cross sectional shapes.

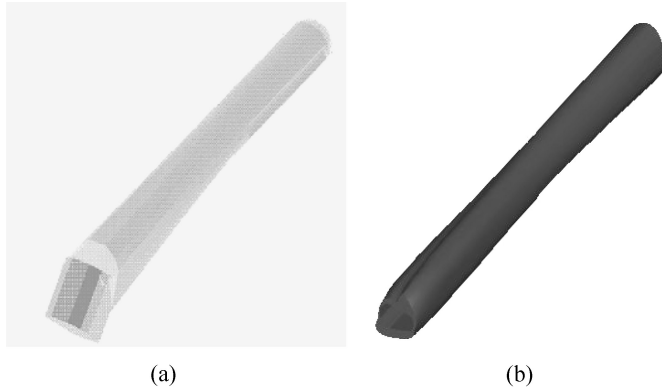


FIG. 5. Solid model of (a) the implant, and (b) the interfacial cement mantle.

implant. This is achieved by extruding the outer surface of the cement over the length of the implant.

3. MATERIAL PROPERTIES FOR THE BONE, CEMENT AND IMPLANT

Several studies have determined elastic properties of bone [20–24]. Relatively few studies have, however, characterized the degree of anisotropy or reported the elastic properties of bone as a function of the anatomical position in the bone. It has been suggested in [19, 21] that assumptions of relatively high material symmetry, e.g. transverse isotropy or orthotropy, are sufficient for stress analysis of the bone.

The present study uses orthotropic elastic property data from experimental studies conducted in Ashman et al. [11] to construct anisotropic elastic property maps as functions of location in the bone. In [11], cubic specimens of the bone were extracted from various points along the length of a canine femur in each of the anterior, medial, posterior, and lateral quadrants (see Figs. 6 and 7) and a continuous wave technique was applied for

TABLE 1
Average values of orthotropic elastic parameters for the canine femur from Ashman et al. (1984)

Poisson’s ratios	Value	Young’s/Shear moduli	Value
ν_{12}	0.282	E_1	12.8 GPa
ν_{12}	0.289	E_2	15.6 GPa
ν_{23}	0.265	E_3	20.1 GPa
ν_{21}	0.366	G_{12}	4.68 GPa
ν_{31}	0.454	G_{13}	5.68 GPa
ν_{32}	0.341	G_{23}	6.67 GPa

measuring the bone properties in different directions. The method allows for the measurement of wave velocities in the direction of the incident wave and along a direction perpendicular to it. The average values of the elastic constants are provided in Table 1. For orthotropic materials, the reduced order elastic stiffness matrix $[C_{ij}]$ is obtained at each point by inverting the compliance matrix set up using the values of the three elastic moduli and six Poisson’s ratios.

$$[C_{ij}] = \begin{bmatrix} \frac{1}{E_1} & \frac{-\nu_{12}}{E_2} & \frac{-\nu_{13}}{E_3} & 0 & 0 & 0 \\ \frac{-\nu_{12}}{E_1} & \frac{1}{E_2} & \frac{-\nu_{23}}{E_3} & 0 & 0 & 0 \\ \frac{-\nu_{13}}{E_1} & \frac{-\nu_{23}}{E_2} & \frac{1}{E_3} & 0 & 0 & 0 \\ 0 & 0 & 0 & \frac{1}{G_{13}} & 0 & 0 \\ 0 & 0 & 0 & 0 & \frac{1}{G_{11}} & 0 \\ 0 & 0 & 0 & 0 & 0 & \frac{1}{G_{12}} \end{bmatrix}^{-1} \quad (1)$$

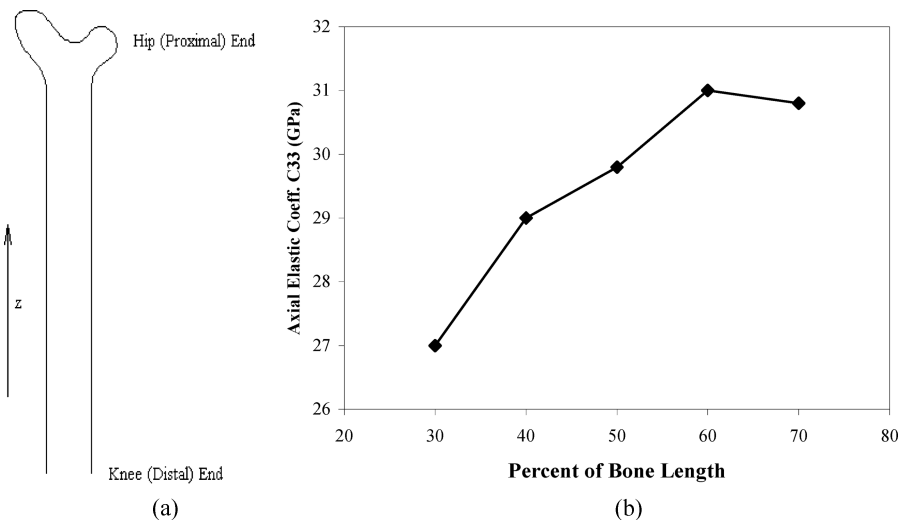


FIG. 6. (a) Direction showing the z axis along the bone; (b) variation of axial elastic coefficient C_{33} along the length of the bone.

Downloaded by [JH Libraries] at 08:41 03 August 2016

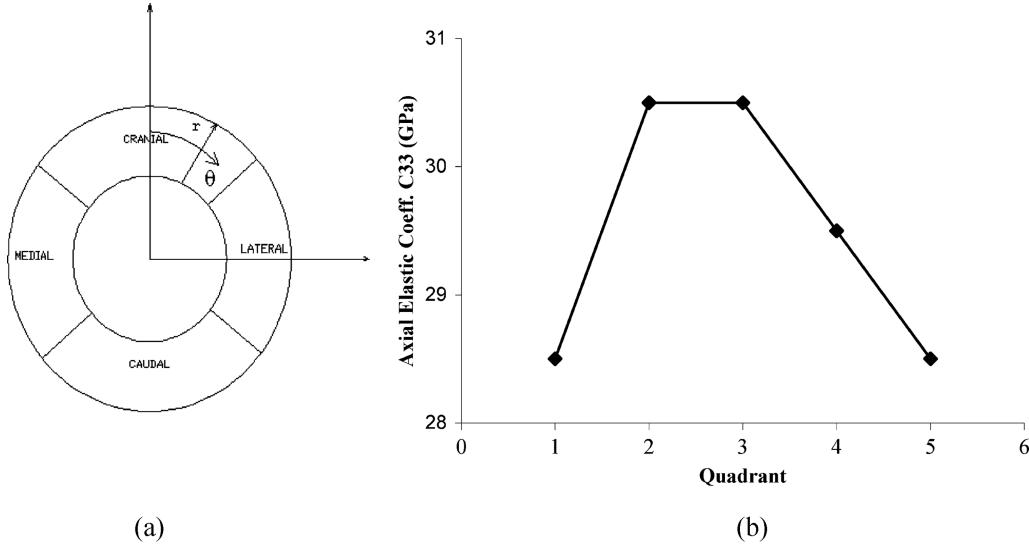


FIG. 7. (a) Direction showing the θ axis along the circumference; (b) variation of elastic coefficient C_{33} along the circumference of the bone.

Variation of the elastic stiffness coefficient C_{33} (3 being the axial direction in the femur) along the length of the bone and along the circumference are provided in [15], shown in Figs. 6 and 7, respectively. The stiffness coefficients C_{ij} are evaluated with the assumption that the variation of all coefficients on the spatial coordinates r , θ and z , are the same, since they all depend on the local microstructural material morphology. The following steps are used for constructing the stiffness matrix.

- (i) A functional form of the variation of C_{33} with the spatial coordinates r , θ and z is created, where r ($0 \leq r \leq 1$) corresponds to a scaled radial coordinate, θ ($0 \leq \theta < 2\pi$) is the angular coordinate measured from the center of the cranial quadrant and z ($0 \leq z \leq 100$) is the scaled position along the length from the distal end to the proximal end. The variations in different directions are obtained from experimental observations in Nelson et al. (1995) by using a least square fit.

$$C_{33}(r, \theta, z)_{r=0, \theta=0} = (-0.00007z^3 + 0.0078z^2 - 0.1021z + 25.514) \text{ GPa} \quad (2a)$$

$$C_{33}(r, \theta, z)_{r=0, z=50} = (-0.04317\theta^3 - 0.06085\theta^2 + 2.12311\theta + 28.50) \text{ GPa} \quad (2b)$$

$$C_{33}(r, \theta, z)_{\theta=0, z=50} = (0.02r + 28.818) \text{ GPa} \quad (2c)$$

The functional form of the coefficient is expressed by superposition of the individual functions as

$$C_{33}(r, \theta, z) = (k_0 + 0.02r - 0.04317\theta^3 - 0.06085\theta^2 + 2.12311\theta - 0.00007z^3 + 0.0078z^2 - 0.1021z) \text{ GPa} \quad (3)$$

The constant k_0 is evaluated from the average value $\overline{C_{33}} = \frac{\int_0^1 \int_0^{2\pi} \int_0^{100} C_{33}(z, \theta, r) dz d\theta dr}{\int_0^1 \int_0^{2\pi} \int_0^{100} dz d\theta dr}$ calculated from the constants in Table 1, from which k_0 is 27.09.

- (ii) The expressions for all the other stiffness coefficients C_{ij} ($i \neq 3, j \neq 3$) are obtained by scaling the expression in Eq. (3) in proportion to the ratio of the average values $\frac{\overline{C_{ij}}}{\overline{C_{33}}}$. For example, since the ratio of the average values of $\frac{\overline{C_{11}}}{\overline{C_{33}}}$ is 0.6397,

$$C_{11} = (17.33 + 0.012r - 0.0276\theta^3 - 0.0389\theta^2 + 1.358\theta - 0.000045z^3 + 0.0049z^2 - 0.653z) \text{ GPa} \quad (4)$$

The plots of C_{11} and C_{33} for $r = 0$ are shown in Fig. 8. These properties are used in the finite element analysis of the bone.

The cement material polymethylmethacrylate (PMMA) has a lower elastic modulus than the bone and the metal prosthesis. The cement is assumed to be homogeneous and isotropic linear elastic and the mechanical properties are taken from [25] as $E_{\text{cement}} = 2.173 \text{ GPa}$ and $\nu_{\text{cement}} = 0.25$. Cobalt-chrome alloy, known for its high modulus and corrosion resistance, is used in

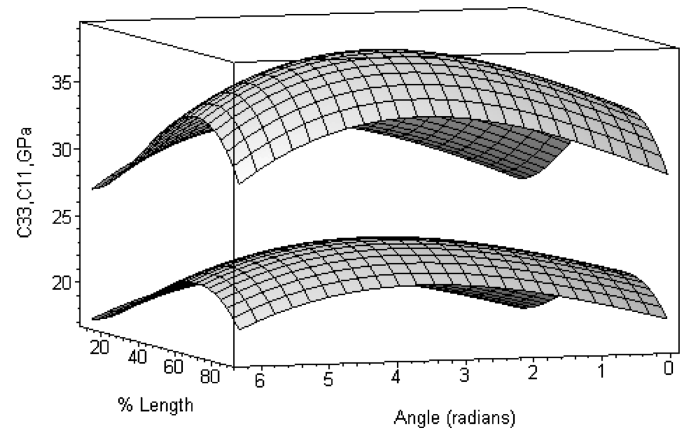


FIG. 8. Plots of C_{11} and C_{33} for $r = 0$ as functions of the position along the bone.

Biomedtrix implants. The elastic properties are obtained from ASM metals handbook [26] as $E_{\text{implant}} = 248 \text{ GPa}$ and $\nu_{\text{implant}} = 0.30$.

4. MACROSCOPIC FE MODEL OF THE BONE-CEMENT-IMPLANT ASSEMBLY

A 3D macroscopic finite element model of the bone-cement-implant assembly is developed for analysis with the ABAQUS-Standard code. Similar 3D studies of femoral bone and cement implant systems have been presented in [28–32]. The present analyses are used to understand the effects of design changes made to a Biomedtrix manufactured implant, on the stresses developed in the bone-implant-cement assembly.

4.1. The Finite Element Mesh

Components of the bone-cement-implant assembly exhibit large dimensional disparities. The cortical bone in the proximal region has a thickness of about 1 mm~1.5 mm, whereas the cement mantle in this region is about 2 mm wide, and the implant diameter is 7 mm to 9 mm. Due to the non-uniform cross section of the components, this thickness varies along the length of the bone towards the mid-diaphysis, where the cortex has a thickness of 2 mm to 2.5 mm, cement has a thickness of 2.5 mm to 3 mm, and the implant has a diameter of 6 mm to 8 mm. To provide appropriate resolution to the finite element mesh for each component in the assembly, the following steps are executed.

- (i) The CAD models of the bone, implant, and cement are loaded in I-DEAS™ “parts library.” The Master Assembly module is then invoked and parts are recalled from the library into the assembly.
- (ii) The cement mantle is assembled with the bone, by aligning the proximal surfaces of the cement and the bone. The implant is then inserted into the assembly by aligning the implant lateral flat surfaces and the cement inner surface. Fine adjustments are made to the assembly by zooming into specific points and using the “coincident points” and “coincident surface” options to connect regions. Initially the biggest size of the implant that can be accommodated, allowing for a minimum cement mantle of 2 mm in the bone proximal region, is assembled. The implant is positioned such that the distal tip is centrally located, providing a uniform cement mantle in the femoral distal region.
- (iii) Element resolution and continuity between the components necessitates further subdivision of the individual domains of the bone-cement-implant system. The bone is subdivided into two annular regions throughout its entire length, viz. an inner region contiguous to the bone-cement interface with a radial thickness of 0.38 mm and an outer region with an average radial thickness of ~2.88 mm. Similarly, the cement mantle is subdivided into three contiguous sub-

layers with an outer layer thickness of 0.38 mm at the bone-cement interface and an inner layer of thickness 0.76 mm at the cement-implant interface. The dimensions of the sub-layers are arrived at iteratively, in attempting to achieve elements with moderate aspect ratios.

- (iv) The meshing module in I-DEAS™ is invoked for discretization in the manual-meshing mode. The four-noded tetrahedron solid element C3D4 in ABAQUS is chosen. The inner region of the implant is discretized into elements of minimum size of 0.76 mm, resulting in 4 elements across the thickness at the distal end and 8 to 10 elements in the proximal region. The outer region of the implant and the inner region of the cement have a maximum element size of 0.38 mm with two elements across the thickness. The central sub-layer of cement is discretized using elements of minimum size 0.38 mm, while the outer sub-domain is meshed with elements of maximum size 0.38 mm. Similarly, the inner layer of the bone is discretized into elements of maximum size 0.38 mm and the outer layer into elements of minimum size 0.38 mm. A tolerance of 0.0038 mm is provided for merging the nodes in I-DEAS™. The finite element mesh for each component is shown in Figs. 9a, b and c. The entire model has 138, 493 C3D4 elements with 84127 nodes.

4.2. Load and Boundary Conditions

The average weight of a Rottweiler, whose femur is analyzed in this study, ranges from 110 lbs to 150 lbs. The body weight is distributed such that 40% is on the fore limbs and 60% is on the hind limbs when in the state of rest. However this distribution may vary depending on the gait of the dog with the hind limbs taking 65%–80% of body weight during running. Two sets of stress analyses corresponding to a simulated dynamic compression test and a torsion test are performed in this study.

- (i) Dynamic compression test: A static compressive load of 49.5 lbs. (220.22 N) on each femoral assembly corresponds to a hind leg static analysis with a slightly excess (~10%) load. A step load of four times the static load or 198 lbs. (880.89 N) is applied to represent the dynamic conditions of a running dog. The load is applied as a step function over a 10 seconds interval. The average pressure on the proximal cross sectional area of the implant is 36.7 MPa.
- (ii) Torsion test: A torque of 210.09 N-mm is applied on the top of the cross section of the femur assembly. This corresponds to a twisting moment generated by a frictional force developed due to the static compressive load above, using a Coulomb’s friction coefficient of 0.30. The effective friction force is assumed to be acting at a distance of $(2/3)r$ from the centroid of the implant, where r is the distance of the medial edge from the centroid of the implant. The loads are applied on the implant and the distal femur is fixed, preventing all translations.

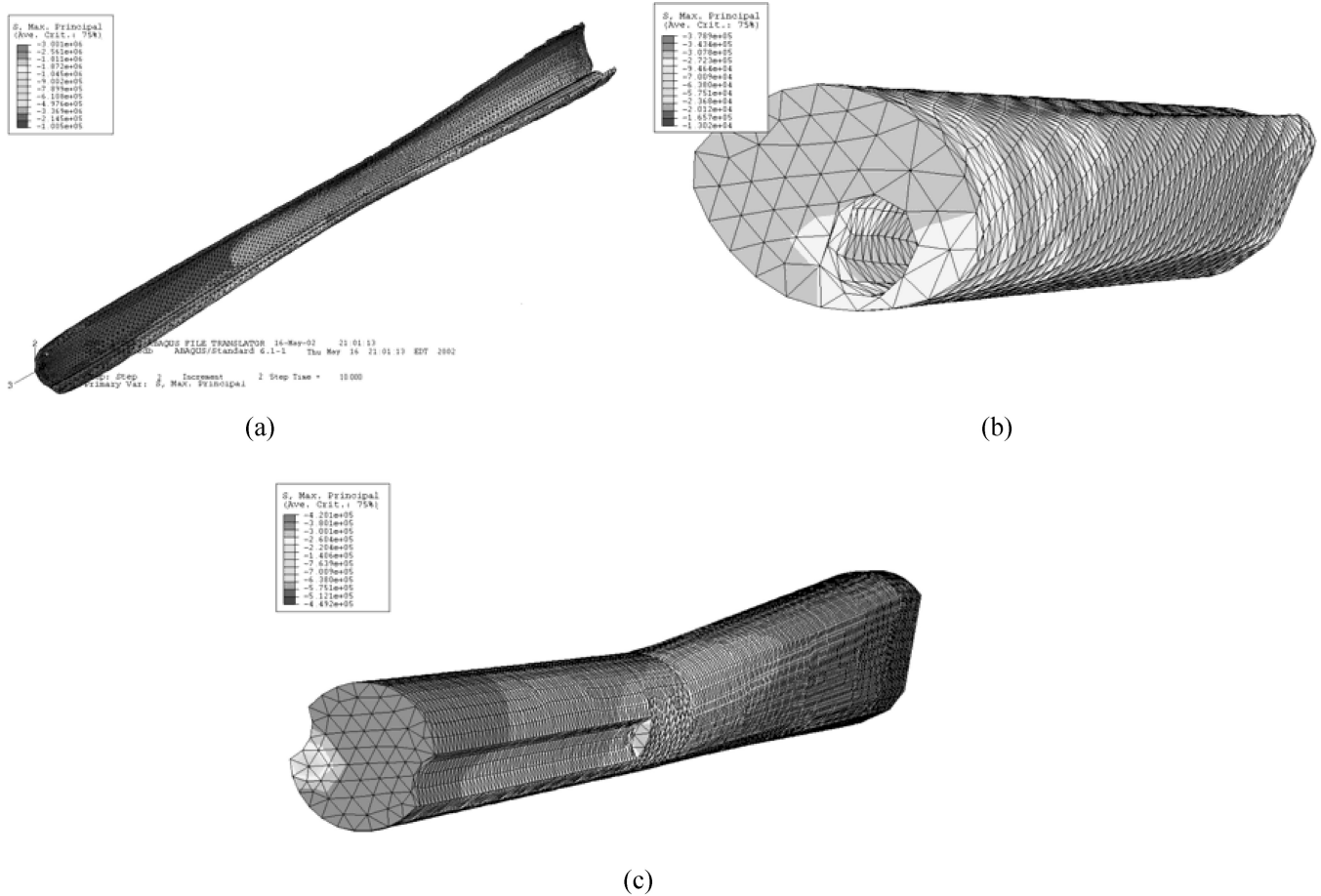


FIG. 9. Maximum principal stress contour plots for the static compression test in (a) the bone; (b) the cement mantle; (c) the implant.

5. RESULTS OF MACROSCOPIC SIMULATIONS

The maximum principal stress contours in the bone, cement mantle, and the implant for the compression and torsion tests are selectively plotted in Fig. 9 and key observations are presented in Tables 2–4. For the compression test, the maximum principal stress in the bone occurs at a distance of 95.1 mm from the proximal end of the bone and in the caudal quadrant of the diaphysial region. This location is about 2.5 mm from the distal tip of the implant. The location of the high stress matches observations of bone-cement-implant failures in practice. The

maximum shear stress occurs at a distance of 90.1 mm from the proximal end of the implant and in the anterior quadrant. For the cement mantle, the stresses are generally uniform across the cross section, with the maximum stress occurring at the distal tip of the implant in the cranial and caudal quadrants, around the cement pockets. The compressive stress in the implant is also relatively uniform with the maximum principal stress occurring at the distal tip in the caudal quadrant. A high stress region or H.S.R in Tables 2–4 is an indicator of the extent of high stresses, and is defined as the fraction of the entire domain

TABLE 2
Normal and shear stresses for static compression test

	Normal stress (kPa)				Shear stress (kPa)			
	Avg. (E + 05)	Max. (E + 05)	Min. (E + 03)	H.S.R %	Avg. (E + 05)	Max. (E + 05)	Min. (E + 03)	H.S.R %
Bone	-4.132	-7.25	-1.003	0.987	2.045	3.122	0.981	0.481
Cement	-2.002	-3.91	-2.136	0.808	1.002	1.896	0.675	0.501
Implant	-2.889	-4.401	-1.134	0.611	0.894	1.416	0.441	0.389

TABLE 3
Normal and shear stresses for static torsion test

Component	Normal stress (kPa)				Shear stress (kPa)			
	Avg. E + 05	Max. E + 05	Min. E + 03	H.S.R %	Avg. E + 05	Max. E + 05	Min. E + 03	H.S.R %
Bone	0.888	1.008	4.434	0.515	0.916	2.112	0.516	0.624
Cement	0.188	0.609	3.976	0.732	0.385	0.944	0.108	0.773
Implant	0.261	0.412	0.179	0.606	0.311	0.711	0.284	0.591

that is at or above 90% of the maximum corresponding stress level (principal stress or shear stress). The table shows that the HSR is significantly higher in the bone compared to the other components.

For the torsion test results presented in Table 3, the maximum principal stress in the bone occurs at a distance of 91.8 mm from the proximal end and in the anterior quadrant of the diaphysial region. The shear stresses dominate in this test, with the maximum stress occurring over a distance of 90.2 mm to 92.4 mm from the proximal end, in both the cranial and caudal quadrants. The location is at the distal end of the stem near the cement pockets. For the cement mantle the maximum shear stress occurs over a distance of 89.4 mm to 91.3 mm from the proximal end and in the cranial and caudal quadrants around the cement pockets. About 0.8% of the cement mantle lies in the high shear stress region. The high stresses near the cement pockets indicate that the design of the cement pockets affect the overall stress patterns for torsion. The shear stresses in the implant occur in the region of the cement pockets in the cranial and caudal quadrants of the distal stem and are relatively low compared to the bone and cement.

5.1. Macroscopic Sensitivity Studies with Design Parameters

Sensitivity studies are conducted with the macroscopic FEM model to understand the effects of design changes on the macroscopic stress distribution in the bone-cement-implant assembly. Simulations are conducted for the dynamic compression conditions. Three design parameters are chosen based on BioMedtrix's

requirements, namely: (a) the length of the distal taper (l), (b) the depth of the cement pocket (r), and (c) the cross section of the implant as shown in Fig. 4. Major results with the design changes are summarized in Table 5. The numbers in the parenthesis indicated the increase or decrease in the stresses or H.S.R due to the design changes.

The distal taper length (l) is changed by $\pm 10\%$. The increase in the length reduces the peak value of the maximum principal stress and also the regions of high stress (HSR) in all components of the assembly, which produces desirable effects in the assembly. Furthermore, the location of the maximum stress moves distally. The effect on the shear stresses is marginal. The decrease in the length of the distal taper increases the peak value of the maximum principal stress in the bone, cement, and implant but the region of high stress (HSR) in all the three components is smaller. This indicates that a shorter taper produces a higher local stress, but its effect is over a smaller region. Next, the depth of the cement pockets (r) is changed by $\pm 3.5\%$. Increase in the depth decreases the stresses in the bone and also reduces the high stress region. However the peak value of the maximum stress and the shear stresses increases in the cement mantle. The effect on the implant is relatively small. Decreasing the depth of the cement pocket has marginal effect in reducing the stresses in the three components and also the HSR. Finally, the cross section of the implant is modified (reduced by 7.5%) as shown in Fig. 4b (iii). This produces highly adverse effects in the components, increasing the stresses and the high stress regions in the bone, cement and implant. Thus this modification is not desirable. The study of the design changes indicates that the use of an implant

TABLE 4
Comparison of normal and shear stresses for dynamic compression test

Component	Normal stress (kPa)				Shear stress (kPa)			
	Avg. E + 06	Max. E + 06	Min. E + 04	H.S.R %	Avg. E + 06	Max. E + 06	Min. E + 05	H.S.R %
Bone	-2.100	-3.21	-0.981	1.322	0.765	1.006	0.442	0.538
Cement	-0.475	-1.71	-0.484	1.051	0.307	0.743	0.289	0.746
Implant	-0.816	-1.267	-4.001	0.811	0.271	0.711	0.306	0.513

TABLE 5
Effects of implant design changes for dynamic compression test

Design parameter	Bone		Cement mantle		Implant	
	Max. Prin. Stress * E + 06 (differ.)	H.S.R (%) (differ.)	Max. Prin. Stress * E + 06 (differ.)	H.S.R (%) (differ.)	Max. Prin. Stress * E + 06 (differ.)	H.S.R (%) (differ.)
Longer distal taper	-3.172 (-1.2%)	0.93 (-29.6%)	-1.688 (-1.29%)	0.89 (-15.3%)	-1.110 (-12.4%)	0.76 (-6.2%)
Shorter distal taper	-3.502 (+9.01%)	0.82 (-37.9%)	-1.743 (+1.93%)	0.91 (-13.4%)	-1.309 (+3.3%)	0.80 (-1.4%)
Deeper cement pocket	-3.152 (-1.81%)	1.01 (-23.6%)	-1.811 (+5.91%)	1.01 (-3.9%)	-1.259 (-0.6%)	0.79 (-2.67%)
Shallow cement pocket	-3.118 (-2.86%)	0.87 (-34.1%)	-1.671 (-2.28%)	0.91 (-13.4%)	-1.169 (-7.7%)	0.82 (+1.1%)
Modified cross section	-3.751 (16.84%)	1.43 (+8.17%)	-1.739 (+1.7%)	1.12 (+6.6%)	-1.323 (+4.4%)	0.98 (+20.8%)

with a longer distal taper suitably modifies the stress state in the bone-cement-implant assembly. It produces a smaller region of high stress and also lowers stress concentrations.

6. DEVELOPMENT OF A MICROSTRUCTURAL BONE MODEL

Image based modeling of the bone microstructure has gained a significant amount of attention in the recent years with advancements in computing power and technology [33, 34]. This section discusses a systematic procedure for the development of a microstructural analysis model of the bone incorporating actual morphological features. The process encompasses acquisition of microstructural data from histological serial sectioning, obtaining 3D renderings of the microstructure, an inverse

method of bone property determination and stress analysis at various locations.

6.1. Histology and Microstructural Data Acquisition

The 3D morphology of the porous bone microstructure is obtained by histology or serial sectioning method of gradual removal of parallel layers of bone material. It is a method used for accurate 3-D microstructure visualization at the resolution of the micro-porosity size and spacing. Some of the key elements in the histology process are:

- (i) Near-cylindrical slices of bone of 5 mm thickness are extracted from different locations along its length, as shown in Fig. 10a. Each of these slices is sub-sectioned into the

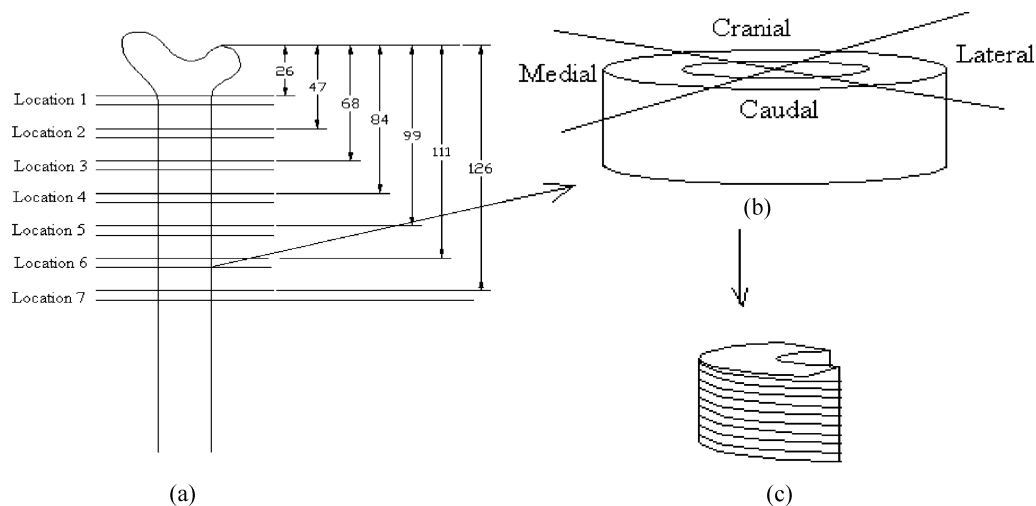


FIG. 10. Schematic of the histology process: (a) locations along the femur for slicing; (b) a typical slice with circumferential regions; and (c) quadrant showing multiple histology sections.

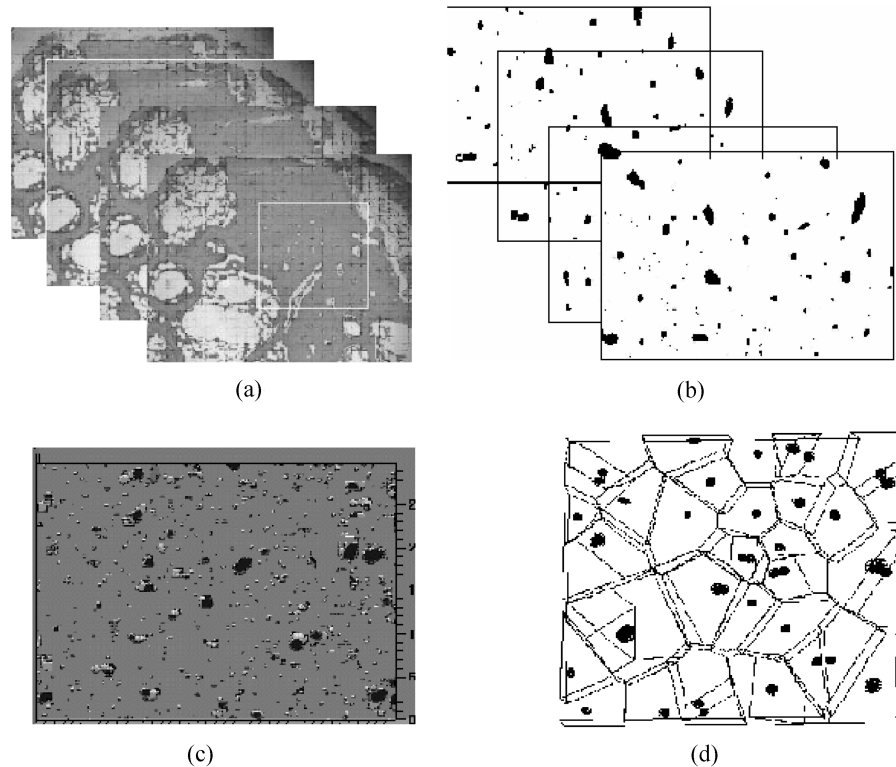


FIG. 11. (a) Stack of micrographs of sections obtained by histology; (b) filtered regions of black and white images of voids; (c) 3D volume rendering from assembled sections; (d) equivalent microstructure tessellated into Voronoi cell network.

cranial, lateral, caudal and medial quadrants. The blocks are decalcified with 8% formic acid/hydrochloric acid (1:1 v/v). The decalcified blocks are processed for paraffin embedding.

- (ii) The slices in each quadrant are serially sectioned at $7\ \mu\text{m}$ thickness using a microtome. Each section is mounted on a glass slide and stained.
- (iii) Stained sections are observed under a SPOT optical microscope [35], consisting of a digital camera mounted on a microscope and connected to a computer with image analysis software SPOT 6.1. Approximately 25 to 30 consecutive images are obtained from each quadrant at each location, as shown in Fig. 11a.

6.2. 3D Microstructure Reconstruction

3D microstructures are computationally reconstructed by sequential assembly of all sections that are digitized from the 2D histology images. 2-D section micrographs are stacked in parallel and a volume rendering software *Slicer-Dicer 3.5* [36] is used to interpolate between the slices to obtain final 3-D microstructure shown in Fig. 11c. Accurate alignment of the parallel slices is achieved using *Adobe Photoshop* in which the contour of a single void and an edge are matched. The dimensions of the microstructural blocks are typically $\sim 250\ \mu\text{m} \times 180\ \mu\text{m} \times 50\ \mu\text{m}$.

The 3D model is digitized and is processed for microstructural modeling.

6.3. Computer Simulated Equivalent Bone Microstructure

The actual 3D microstructural geometry in Fig. 11c is generally quite complex and an exhaustive database is required to store all the geometric details. To avert this, equivalent microstructures that closely approximate the actual morphology but are computationally less demanding are generated. In this process, each void of arbitrary morphology is replaced by an equivalent ellipsoid. This process economizes the image analysis and characterization process by way of well-known geometric properties of ellipsoids. The digitized image data are first transferred into binary format to distinguish between the porosity and bone material phases. The 0-th (I_0), 1st (I_x, I_y, I_z) and 2nd ($I_{xx}, I_{yy}, I_{zz}, I_{xy}, I_{yz}, I_{xz}$) order geometric moments are then computed for each void by adding the contributions from each voxel that lie within the void boundary. The centroidal coordinates (x_c, y_c, z_c) of the equivalent ellipsoid are first evaluated from the zero and first order moments as:

$$x_c = I_x / I_0, y_c = I_y / I_0, z_c = I_z / I_0 \quad (5)$$

The major, intermediate, and minor axes of the equivalent ellipsoids are then obtained from the principal moments I_1, I_2, I_3 as:

$$a = \sqrt{\frac{5}{I_0}(I_2 + I_3 - I_1)}, \quad b = \sqrt{\frac{5}{I_0}(I_1 + I_3 - I_2)},$$

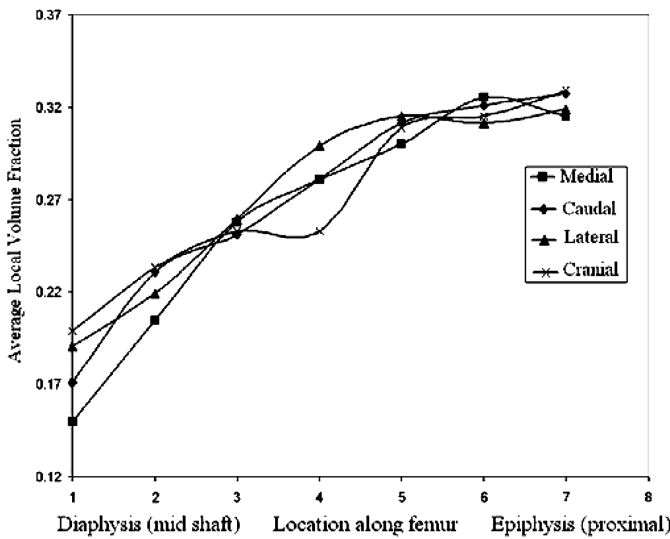
$$c = \sqrt{\frac{5}{I_0}(I_1 + I_2 - I_3)} \quad (6)$$

The principal directions (or orientations of the three axes) for the ellipsoids are obtained from the eigenvalues of the second order

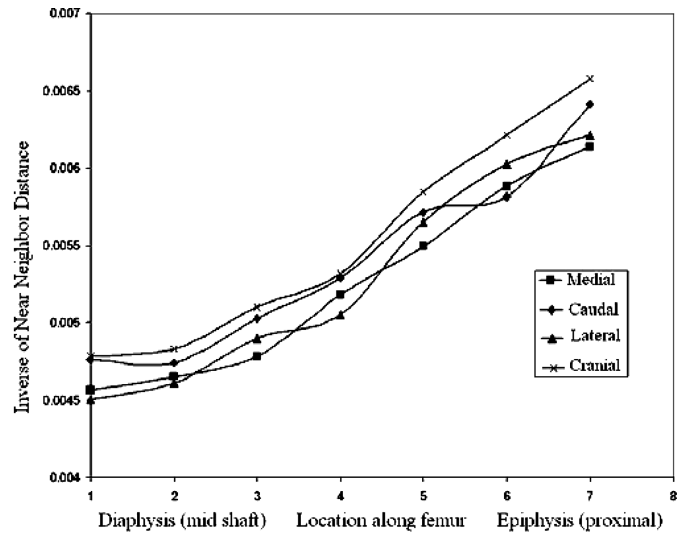
moments $I_{ij} (i = 1..3, \text{ and } j = 1..3)$. A computer simulated 3D equivalent microstructure is shown in Fig. 11d.

6.4. Tessellation of the Microstructural Domain and Quantitative Characterization

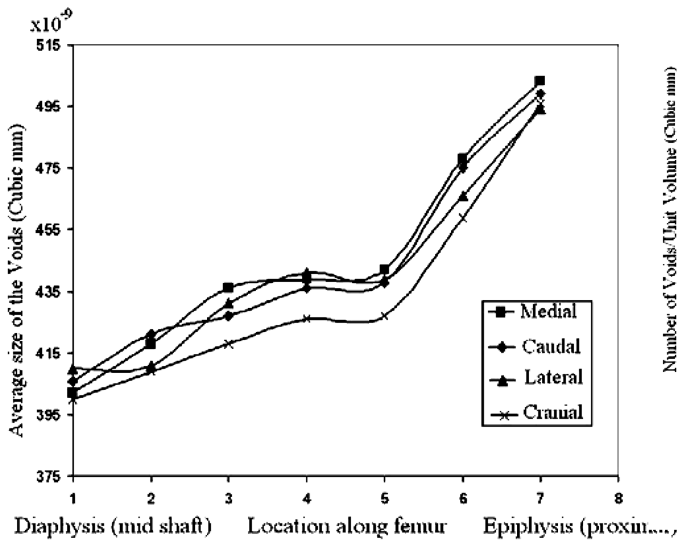
Voronoi tessellation is the subdivision of a heterogeneous region based on the size and location of a set of heterogeneities into Voronoi cells, such that each cell represents the immediate neighbourhood of the heterogeneity. Figure 11d shows a computed equivalent microstructural block tessellated into a mesh of Voronoi elements. The mesh of Voronoi cells plays an important role in the development of geometric descriptors for quantitative



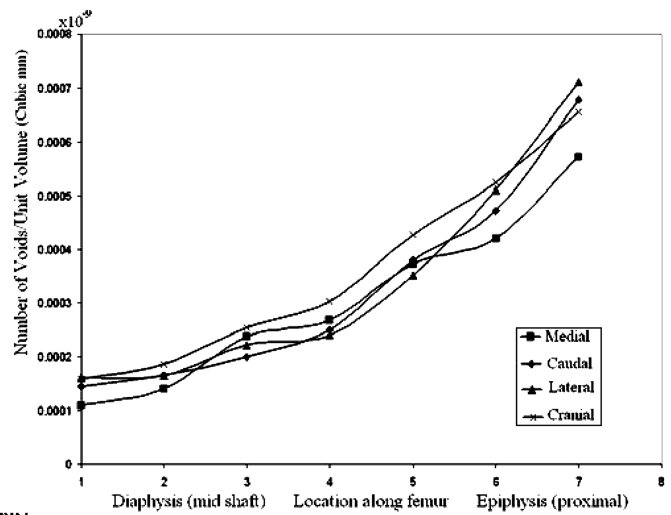
(a)



(b)



(c)



(d)

FIG. 12. Variation of (a) average local volume fraction; (b) average nearest-neighbor distance; (c) average void size; and (d) number of voids per unit volume, along the length of the bone.

characterization of a heterogeneous microstructure, since each cell may be identified as a basic structural element of the microstructure. For a porous material, the cells represent the immediate neighborhood of each void and also define neighboring voids as those which share cell facets. Details of the Voronoi tessellation process in 2D and 3D and quantitative characterization are presented in Li et al. [37, 38].

Following the procedure discussed in [37, 38], the distributions of four different microstructural parameters, namely (a) local volume fraction, (b) nearest neighbor center-to-center distance, (c) size of the voids, and (d) number of voids in each microstructural block of the bone at different locations, are examined in this study. The local volume fraction (V_{VF}) is the ratio of the void size to the size of the associated Voronoi cell, and is a good indicator of the local distribution. The average local volume fraction is evaluated for each of the cranial, caudal, medial, and lateral quadrants and plotted as a function of the distance from the diaphysial region in Fig. 12a. The volume fraction monotonically increases from the diaphysial region to the epiphyseal region, indicating gradually decreasing bone density. The nearest neighbor distance (NND) is an indicator of the local interaction between neighboring voids and can be calculated as the center-to-center distance between voids that share edges of Voronoi cells. In contrast to the local volume fraction, the NND decreases monotonically with distance from the diaphysial region as shown in Fig. 12b due to denser packing of the voids in the epiphyseal region. Variations in the characterization parameters along the bone length are attributed to the adaptation of the bone to the imposed load. The morphology of the femur and its intrinsic structure are a consequence of the modeling in response to the load history (Wolff's law). Regions of the bone subjected to higher compressive load, namely the medial and caudal quadrants are denser. This is reflected in larger nearest neighbor center-to-center distance and smaller volume fractions as compared to the cranial and lateral quadrants of the bone. Figs. 12c and 12d show the variation of the void size and the number of voids per unit volume. It is interesting to note that while the average size of the voids increases in the epiphyseal region, so does the number density.

6.5. An Inverse Method for Elastic Property Evaluation of Pure Bone Material

The mechanical properties of bone are strongly dependent on its microstructural morphology. Variations in the local composition render the overall bone properties highly non-homogeneous. For most micromechanical analyses at the scale of the porosity, it is necessary to input the properties of the bone mass alone without the porosities. This is a challenging task as it requires experiments to be devised at this scale. Nanoindentation techniques, e.g. in [39], have been used to measure microstructural deformations in the bone. However, these techniques do not provide all the necessary information, e.g. anisotropic coefficients. Alternately, an inverse analysis with computational micromechanics is developed in this paper for evaluation of the

TABLE 6
Elastic properties of the bone at various locations by the inverse micromechanics method

Block			
Location	Quadrant	E_B (GPa)	ν_B
1	Cranial	16.32	0.287
2	Caudal	16.308	0.288
3	Lateral	16.33	0.289
4	Medial	16.311	0.288
5	Lateral	16.299	0.289
6	Cranial	16.322	0.287
7	Caudal	16.307	0.286

Young's modulus E_B and Poisson ratio ν_B of the bone. The micromechanical analysis is conducted using a 3D Voronoi cell finite element model (VCFEM) discussed in Ghosh and Moorthy [40]. The essential steps involved are outlined below.

(1) *Generate Representative Material Elements at Different Locations*: Representative material elements (RME) are set up at seven independent locations as indicated in Table 7 and Fig. 10 to determine material properties at different regions in the femur. The RME construction involves equivalent 3-D microstructure construction as discussed in section 6.1. The finite element mesh for VCFEM analysis of each RME is then constructed by tessellation into Voronoi cells shown in Fig. 11d.

(2) *Apply Boundary and Loading Conditions on the RME*: Stress analysis of the RME is conducted using the VCFEM to evaluate orthotropic elastic stiffness coefficient. In VCFEM periodic boundary conditions are applied on the faces of the RME. For nodes on the boundary, which are separated by the periods (Y_1, Y_2, Y_3) along one or more coordinate directions, displacement constraints are imposed in VCFEM as one of the following:

$$\begin{aligned} \mu_i &= (x_1, x_2, x_3) = \mu_i(x_i \pm k_1 Y_1, x_2 \pm k_2 Y_2, x_3 \pm k_3 Y_3), \\ i &= 1, 2, 3 \end{aligned} \quad (7)$$

TABLE 7
Ratio of microstructural peak to average macroscopic Von Mises stress at different regions of the bone

Block		
Location	Quadrant	Ratio of Von-Mises stresses
1	Cranial	1.576
2	Caudal	1.718
3	Lateral	1.988
4	Medial	2.034
5	Lateral	2.313
6	Cranial	2.645
7	Caudal	2.896

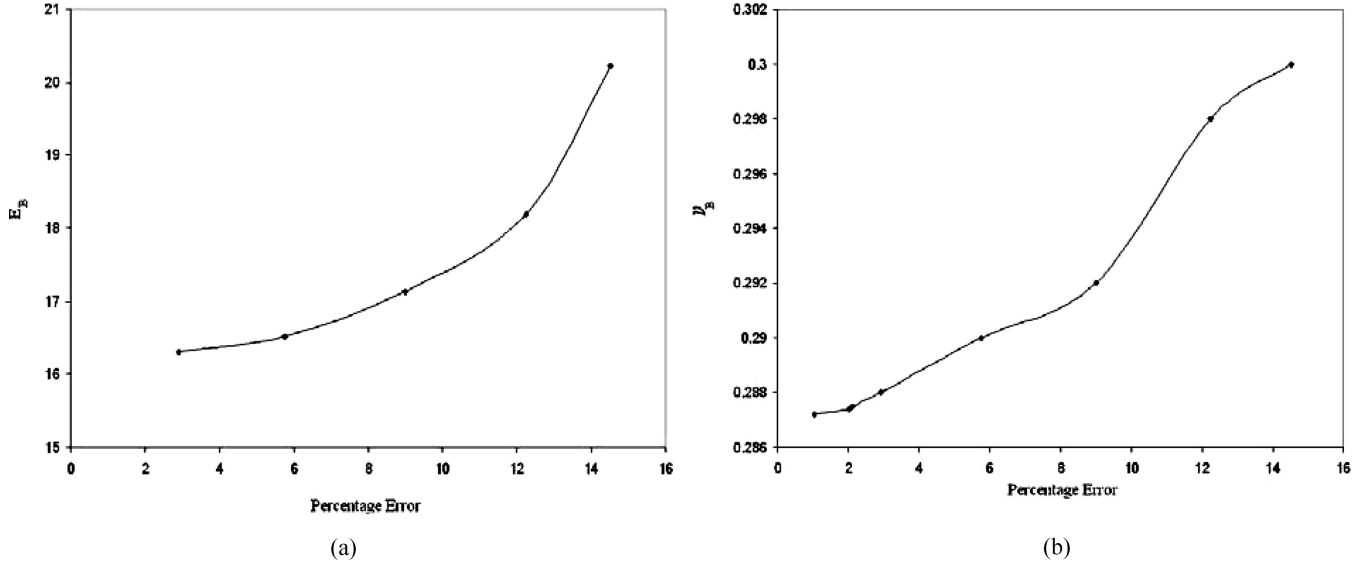


FIG. 13. Convergence plots from inverse analysis of (a) Young's modulus and (b) Poisson's ratio, in the bone material.

where k_1, k_2, k_3 may assume the values 0 or 1, depending on the node locations. The stiffness evaluation process involves solving six sets of RME boundary value problems with these periodic boundary condition and six different applied unit strains corresponding to:

- (a) three normal strains $\varepsilon_{ii} = 1$ (no sum on i) $\forall i = 1, 2, 3$;
 $\varepsilon_{ij} = 0 \forall i \neq j$ and
 (b) three shear strains $\varepsilon_{ij} = 1 \forall i \neq j, i, j = 1, 2, 3$;
 $\varepsilon_{ii} = 0$ (no sum on i) $\forall i = 1, 2, 3$.

(3) *Solve Iteratively the RME Boundary Value Problem:* The linear elastic parameters E_B and ν_B are iteratively evaluated by solving the RME boundary value problem with the boundary conditions in step 2. The volume averaged macroscopic stresses are evaluated from the microscopic stresses in the entire RME as $\overline{\sigma}_{ij} = \frac{\int_{V_{RME}} \sigma_{ij} dV}{\int_{V_{RME}} dV}$. The stress-strain relation is consequently used to evaluate the macroscopic orthotropic coefficients $C_{ij}(r, \theta, z)$ in equation 1. For example, for the case when $\varepsilon_{11} = 1$ and all other strains are zero, $C_{11} = \overline{\sigma}_{11}^{-1}$, $C_{12} = \overline{\sigma}_{22}^{-2}$ and $C_{13} = \overline{\sigma}_{33}^{-1}$. Similarly, for the case when $\varepsilon_{22} = 1$, $C_{22} = \overline{\sigma}_{22}^{-2}$ and $C_{23} = \overline{\sigma}_{33}^{-2}$; for $\varepsilon_{33} = 1$ $C_{33} = \overline{\sigma}_{33}^{-3}$; for $\varepsilon_{12} = 1$ $C_{44} = \overline{\sigma}_{12}^{-4}$, for $\varepsilon_{23} = 1$ $\overline{\sigma}_{23}^{-5}$ and for $\varepsilon_{13} = 1$ $C_{66} = \overline{\sigma}_{13}^{-6}$.

The evaluation process of the material elastic coefficients E_B and ν_B involves iterations to minimize the least square error measure between the simulated values and the experimental values of the stiffness coefficients C_{ij} , following the problem statement

$$\text{Minimize } \sqrt{\sum_{i=1}^6 \sum_{j=1}^6 (C_{ij}^{Expt} - C_{ij}^{Simul})^2} \quad (8)$$

wrt E_B, ν_B

The experimental values of C_{ij} , are discussed in section 3. The iterative process starts with an initial guess of the E_B and ν_B obtained using rule of mixtures. The values of E_B and ν_B are incrementally changed and then input into the VCFEM analysis of the RME boundary value problem. The procedure is repeated till a

$$\% \text{ error} \left(= \frac{\sqrt{\sum_{i=1}^6 \sum_{j=1}^6 (C_{ij}^{Expt} - C_{ij}^{Simul})^2}}{\sqrt{\sum_{i=1}^6 \sum_{j=1}^6 (C_{ij}^{Expt})^2}} \times 100 \right)$$

$< 3\%$ is achieved.

The convergence of the iterative process to the accepted values of the elastic parameters is shown in Fig. 13. Even though the macroscopic properties of the bone vary considerably with location (see Fig. 8), the properties of the bone material are similar, as shown in Table 6. The average Young's modulus of values in Table 5 is 16.31 GPa. The value of E_B has been obtained to be 15.48 GPa for bovine femur bone in [41] by nanoindentation techniques.

7. MICROSTRUCTURAL STRESS ANALYSIS AT VARIOUS FEMORAL LOCATIONS

Image-based microstructural models are increasingly becoming popular for stress analysis in the bone microstructure. Feldkamp et al. [42] have used computed tomography to obtain detailed bone microstructure data. Borah et al. [43] have used magnetic resonance micro-imaging and micro-computed tomography coupled with digital FEM for microstructural analysis. Hollister and Kikuchi [44] have used unit-cell bone models to describe the bone microstructure and homogenization to study bone-remodeling process. Ulrich et al. [45] have evaluated the

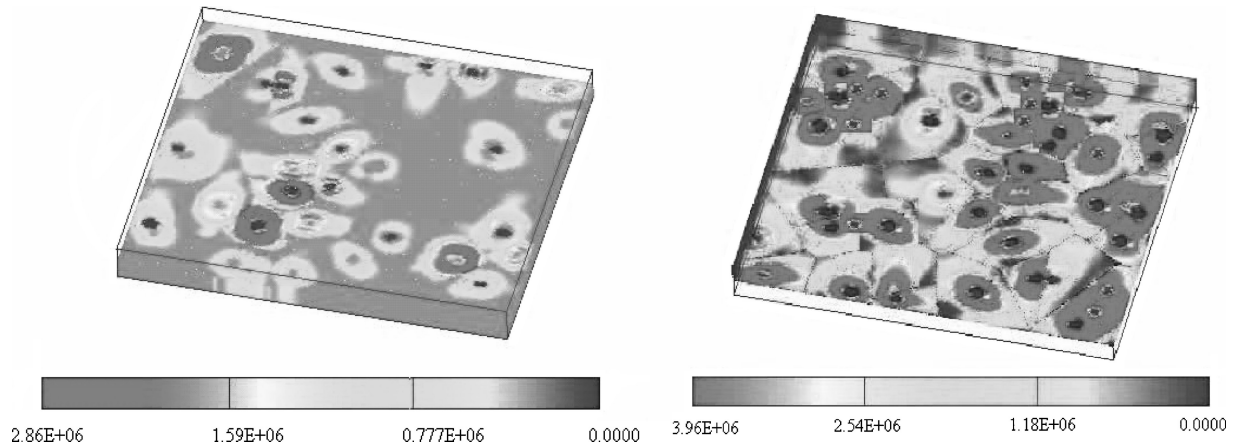


FIG. 14. Contour plots of the Von Mises stress in (a) location 1 of cranial block and (b) location 7 of lateral block.

quality of the trabecular bone with micro-CT and FEA. Parfitt [46] has used bone microstructure models obtained through micro-CT to assess the strength of vertebrae. In the present study, microstructural stress analysis using a 3D Voronoi cell finite element model [40] is used to relate characteristic features of the microstructure to the stress distribution in the bone. The microscopic analyses at various regions of interest in the bone are for the dynamic compression tests discussed in section 5. Seven microstructural blocks of dimensions $\sim 250\mu\text{m} \times 180\mu\text{m} \times 50\mu\text{m}$ from different locations are selected. Macroscopic strains ($\epsilon_x, \epsilon_y, \epsilon_z, \gamma_{xy}, \gamma_{yz}, \gamma_{xz}$) for the compression test are known in elements at these locations from the macroscopic ABAQUS simulations in section 5. Considering the macroscopic strains at each location to be constant, the boundary conditions on the nodes of the microscopic VCFEM model are applied

according to the equations

$$\begin{aligned} u(X, Y, Z) &= \epsilon_{xx}X + \gamma_{xy}Y + \gamma_{xz}Z \\ v(X, Y, Z) &= \epsilon_{yy}Y + \gamma_{yz}Z \\ w(X, Y, Z) &= \epsilon_{zz}Z \end{aligned} \tag{9}$$

where X, Y and Z are the rectangular Cartesian coordinates with its origin at one of the corners of the rectangular RME. The material parameters E_B and ν_B for the VCFEM simulations are taken from Table 5. The Von-Mises stress distribution in the microstructural RME at the cranial block of location 1 and the lateral block location 7 are plotted in Fig. 14. In Fig. 15a the macroscopic Von-Mises stress and the corresponding peak stresses in the microstructure are plotted as functions of macroscopic locations in the femur. The value corresponding to the

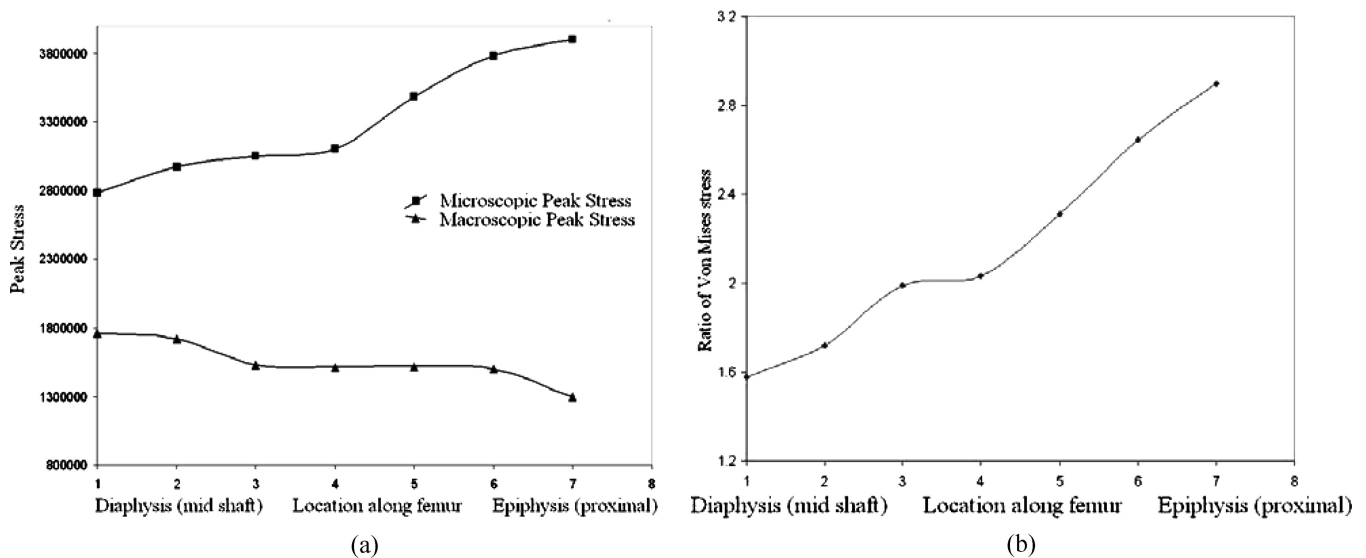


FIG. 15. (a) Peak values of Von-Mises stresses at the microscopic and macroscopic scales and (b) the ratio of the peak microscopic stress along the length of the femur.

diaphysial region represents the maximum macroscopic stress in the bone region analyzed in section 5. While the macroscopic stress reduces from the diaphysial to the epiphysial region, the microscopic peak stress increases significantly in this direction. The reduction in the macroscopic stress is due to the reduction in elastic stiffness towards the epiphysial end. As seen in Fig. 11a, the average void volume fraction monotonically increases from the diaphysis to the proximal epiphysis region, which causes the average elastic modulus to decrease monotonically. On the other hand, the near neighbor distance manifesting the proximity of the voids, decreases in the same direction. This results in an increase in the peak stresses due to thinner ligaments between the voids. Fig. 15b is a plot of the ratio of the peak microscopic stress to the corresponding macroscopic stress. These ratios are quantified in Table 7 for various regions. The ratio varies from 1.6 to 2.9, which suggests that in regions of low near neighbor distance the microscopic stress distribution is significantly higher than what is expected from macroscopic analysis. This significant effect of the microstructural stresses should be taken into account in the design of implants in femur-implant assembly.

8. CONCLUSIONS

This paper presents a comprehensive approach for macroscopic and microscopic analysis of a bonecement-prosthetic implant in a cemented canine hip prosthesis by combining methods of image analysis, microscopy, CAD, mechanical testing, and finite element modeling at multiple scales. In the macroscopic model development and analysis, a systematic approach is developed by coupling various important elements at the macroscopic scale without incorporation of the bone microstructure. These include (a) geometric modeling of the canine femur from computed tomography, (b) reconstruction of the actual canine implant based on the industrial blue-prints, (c) developing a comprehensive material model for the complex bone tissue based on experimental studies, and (d) performing finite element analysis on the bone, cement, implant assembly under realistic loading conditions. The results are post-processed to understand the effects of the component interaction in the bone-implant-cement mantle assembly on the macroscopic stress distribution. A sensitivity analysis is conducted with the macroscopic model to investigate the effect of implant design variables on the stress distribution in the assembly. This is an important outcome of the macroscopic analysis, since the recommendations of this analysis (e.g. a longer distal taper) have a direct impact on the applications.

A rigorous microstructural modeling of the bone is subsequently executed by incorporating a unique combination of several ingredients, viz. (a) microstructural data acquisition of serial sections, (b) 3D image based microstructure reconstruction and simulation, (c) microstructural characterization of the bone microstructure at different locations, (d) an inverse method for determination of the elastic properties of pure bone material, and (e) microstructural stress analysis at various locations. A

number of unique approaches are utilized in the microstructural analysis. Generation of the simulated microstructure and analysis by the 3D Voronoi cell finite element model provides a new way of modeling complex microstructures and correlating to morphological characteristics. The inverse calculation of the material parameters of bone by combining macroscopic experiments with microstructural characterization and analysis is quite unique. It provides a new approach to evaluating bone properties without having to do experiments at this scale. Finally, the microstructural stresses in the femur are computed using the 3D VCFEM to study the stress distribution at the scale of the bone porosity. Significant difference is observed between the macroscopic stresses and the peak microscopic stresses at different locations. The difference is attributed to the variation in the microstructure, e.g. porosity. This should be accounted for in the design process, e.g. when considering proximal design features such as the collar and the design features of the stem tip distally. The pattern of stresses is consistent with many clinical observations. For example, adaptive bone remodeling in the convalescent period after total hip replacement is characterized by periosteal new bone formation localized to the area of high stress in the diaphysis; femoral fatigue fracture after total hip replacement is initiated in high stress region of the diaphysis; aseptic loosening by bone cement interface deterioration is radiographically apparent as endosteolysis near the stem tip; and cement mantle fracture can occur after aseptic loosening at the level of the stem tip [47]. In conclusion, it is hypothesized that significant improvements in computer modeling based design of endoprosthesis can be accomplished with application of multiple-scale analysis.

REFERENCES

- Olmstead, M. L., "The canine cemented modular total hip prosthesis," *J. Amer. Anim. Hosp. Assoc.*, **31**, 109–115 (1995).
- Kavanaugh, B. F., "Charnley total hip arthroplasty with cement, fifteen year results," *Engng. Medic.*, **15**, 19–29 (1989).
- Evans, B. G., Salvati, E. A., Huo, M. H., and Huk, O. L., "The rationale for cemented total hip arthroplasty," *Orthop. Clin. NA.*, **24**, 599–607 (1993).
- Ebramzadeh, E., Sarmiento, A., and McKellop, H. A., "The cemented mantle in total hip arthroplasty," *JBJS-Amer.*, **76**, 77–89 (1994).
- Goldberg, B. A., Al-Habbal, G., and Noble, P. C., "Proximal and distal femoral centralizers in modern cemented hip arthroplasty," *Clin. Orthop. Rel. Res.*, **349**, 163–167 (1998).
- Poss, R., Brick, G. W., Wright, R. J., Roberts, D. W., and Sledge, C. B., "The effects of modern cementing techniques on longevity of total hip arthroplasty," *Orthop. Clin. NA.*, **19**, 591–601 (1988).
- Wylie, K. B., DeYoung, D. J., Drost, W. T., and DeYoung, B. A., "The effect of surgical approach on femoral stem position in canine cemented total hip arthroplasty," *Vet. Surg.*, **26**, 62–76 (1997).
- Namba, R. S., Keyak, J. S., Kim, A. S., Vu, L. P. and Skinner, H. B., "Cementless implant composition and femoral stress, a finite element analysis," *Clin. Orthop.*, **347**, 261–269 (1998).
- Marom, S. A., and Linden, M. J., "Computer aided stress analysis of long bones utilizing computer tomography," *J. Biomech.*, **23**, 399–407 (1990).
- Huang, H. K., Suarez, F. R., and Toridis, T. G., "Utilization of computerized tomography scans as input to finite-element analysis," *Intl. Conf. of Finite Elements in Biomechanics*, **2**, 797–809 (1980).

11. Ashman, R. B., Cowin, S. C., Van Buskirk, W. C., and Rice, J. C., "A continuous wave technique for the measurement of elastic properties of cortical bone," *J. Biomech.*, **17**, 349–359 (1984).
12. Huiskes, R., Strens, P. H. G. E., van Heck, J., and Slooff, T. J. J. H., "Some fundamental aspects of human joint replacement," *Orthop. Scand. Suppl.* **185**, 109–116 (1980).
13. Kwak, B. M., and Yoo, V. V. S., "An investigation of the effect of cement thickness on an implant by finite element stress analysis," *Internat. Orthop.*, **2**, 315–322 (1979).
14. Estok, D. M., Orr, T. E., and Harris, W. H., "Factors affecting cement strains near the tip of a cemented femoral component," *J. Arthroplasty*, **12**, 40–48 (1997).
15. Nelson, P. C., Robertson, D. D., and Walker, J. W., "A computerized femoral intramedullary implant design package utilizing computer tomography data," *IEEE Trans.*, **111**, 200–213 (1995).
16. AUTOCAD 2000, Reference Manual, Autodesk Inc.
17. I-DEAS™, User's Manual, SDRC Inc.
18. BioMedtrix Corporation, Allendale, New Jersey.
19. Huiskes, R., and Chao, E., "A survey of finite element analysis in orthopedic biomechanics: the first decade," *Journal of Biomechanics*, **16**, 385–409 (1983).
20. Cowin, S. C., VanBuskirk, W. C., and Ashman, R. B., *Properties of Bone*. McGraw-Hill, New York (1989).
21. Ashman, R. B., "Ultrasonic determination of properties of cortical bone: techniques and limitations," *PhD Dissertation*, Tulane University, New Orleans, LA (1982).
22. Knetts, I.V., and Malmeisters, A., "The deformability and strength of compact bone tissues," *Mechanics of Biological Solids*, McGraw-Hill, New York (1975).
23. van Rietbergen, B., Weinans, H., Huiskes, R., and Odgaard, A., "A new method to determine the trabecular bone elastic properties and loading using micromechanical finite element models," *Journal of Biomechanics*, **28**, 69–81 (1995).
24. Rho, J. Y., Tsui, T. Y., and Pharr, G. M., "Elastic properties of human cortical and trabecular lamellar bone measured by nanoindentation," *Biomaterials*, **18**, 1325–1330 (1997).
25. McKellop, H. A., "Properties of PMMA cement," *PhD Dissertation*, University of Southern California (1988).
26. *ASM Metals Handbook*, McGraw-Hill, New York (1999).
27. *ABAQUS/Standard, Version 6.1*, User's Manual, Hibbitt, Karlsson & Sorensen Inc, Pawtucket, Rhode Island, 2002.
28. Valliappan, S., Svensson, N. L., and Wood, R. D., "Three dimensional stress analysis of the human femur," *Comput. Biol. Med.*, **7**, 253–262 (1977).
29. Hampton, S. J., Andriacchi, T. P., and Galante, J. O., "Three dimensional stress analysis of the femoral stem of a total hip prosthesis," *J. Biomechanics*, **13**, 443–454 (1980).
30. McNamara B. P., Cristofolini, L., Aldo, T., and Taylor, D., "Relationship between bone-prosthesis bonding and load transfer in total hip reconstruction," *J. Biomechanics*, **30**, 621–633 (1997).
31. Rakatomanana, L. R., Terrier, A., Ramaniraka, N. A., and Leyvraz, P. F., "Anchorage of orthopedic prosthesis: influence of bone properties and bone implant mechanics," *Synthesis in Bio Solid Mechanics*, P. Pedersen and M. P. Bendsoe (eds.), Kluwer Acad. Publishers, 55–66 (1999).
32. Maldonado, Z. M., Bendayan, J., and Kinzbrunder, D., "Comparative analysis of the geometrical design parameters in cemented hip prosthesis," *Proceedings of Eccomas 2000*, Barcelona, September 2000.
33. Niebur, G. L., Feldstein, M. J., Yuen, J. C., Chen, T. J., and Keaveny, T. M., "High resolution finite element models with tissue strength asymmetry accurately predict failure of trabecular bone," *J. Biomech.*, **33**(12), 1575–1583 (2000).
34. Guldborg, R. E., Hollister, S. J., Charras, G. T., "The accuracy of digital image-based finite element models," *J. Biomech.*, **120**(4), 289–295 (1998).
35. SPOT, Version 6.1, User's Manual, 1999.
36. Slicer-Dicer, Version 3.5, User's Manual, Pixotech Corporation, 1999.
37. Li, M., Ghosh, S., Richmond, O., Weiland, H., and Rouns, T. N., "Three dimensional characterization and modeling of particle reinforced MMCs, Part I: Quantitative description of microstructural morphology," *Mater. Sci. Engin. A.*, **A265**, 153–173 (1999).
38. Li, M., Ghosh, S., Richmond, O., Weiland, H., and Rouns, T. N., "Three dimensional characterization and modeling of particle reinforced MMCs, Part II: Damage characterization," *Mater. Sci. Engin. A.*, **A266**, 221–240 (1999).
39. Rho, J. Y., and Pharr, G. M., "The nanoindentation properties of herring bone related to microstructure," *Bone Mechanics*, **15**, 34–41 (1998).
40. Ghosh, S., and Moorthy, S., "Three dimensional Voronoi cell finite element model for modeling microstructures with ellipsoidal heterogeneities," *Comput. Mech.*, **34**(6), 510–531 (2004).
41. Fan, Z., Rho, J. Y., "Nanoindentation properties of bovine and human cortical bone," *Annual Meeting, Orthopedic Research Society*, 63–68 (1999).
42. Feldkamp, L. A., Goldstein, S. A., Parfitt, A. M., and Jasion, G., "The direct examination of three dimensional bone architecture in vitro by computed tomography," *J. Bone Miner. Res.*, **4**, 3–11 (1997).
43. Borah, B., Gross, G. J., Dufresne, T. E., Chmielewski, P. A., Lundy, M. W., and Sod, E. W., "Three dimensional micro-imaging, finite element modeling and rapid prototyping provide unique insights into bone architecture in osteoporosis," *The Anat. Rec.*, **265**, 101–110 (2001).
44. Hollister, S. J., and Kikuchi, N., "Homogenization theory and digital imaging: A basis for studying the mechanics and design principles of bone," *Biotech. Bioengng.*, **43**, 586–596 (1994).
45. Ulrich, D., Hilderbrand, T., Rietbergen, V., and Muller, R., "The quality of trabecular bone evaluated with micro-CT, FEA and mechanical testing," *Bone Research Biomechanics*, **1**, 97–111 (1997).
46. Parfitt, A. M., "Implications of architecture for prevention of vertebral fracture," *Bone*, **13**, 41–47 (1996).
47. Marion, N. W., et al. "Borate glass supports the in vitro osteogenic differentiation of human mesenchymal stem cells," *Mechanics of Advance Materials and Structures*, **12**(3), 239–244 (2005).